Assessment of Sentinel-3 Altimeter Performance over Antarctica using High Resolution Digital Elevation Models

Joe Phillips[1] and Malcolm McMillan[1]

[1]UK Centre for Polar Observation and Modelling, Centre of Excellence in Environmental Data Science, Lancaster Environment Centre, Lancaster University, Lancaster, UK

Correspondence: Joe Phillips (j.phillips5@lancaster.ac.uk)

Abstract. Since 2016, the Sentinel-3 satellites have provided a continuous record of ice sheet elevation and elevation change. Given the unique, operational nature of the mission, and the planned launch of two additional satellites before the end of this decade, it is important to determine the performance of the altimeter across a range of ice sheet topographic surfaces. Whilst previous studies have assessed elevation accuracy, more detailed investigations of the underlying instrument and processor performance are lacking. This study therefore examines the performance of the Sentinel-3 Synthetic Aperture Radar (SAR) altimeter over the Antarctic Ice Sheet (AIS), utilising new detailed topographic information from the Reference Elevation Model of Antarctica (REMA). Applying Singular Value Decomposition to REMA, we firstly develop new self-consistent Antarctic surface slope and roughness datasets. We then use these datasets to assess altimeter performance across different topographic regimes, targeting a number of key steps in the altimeter processing chain. We also evaluate the impact of topography upon waveform decorrelation. We find that, for 90% of acquisitions, the point of closest approach to the satellite is successfully captured within the Level-1b range window. However, performance degrades with increasing topographic complexity, and this also affects the capacity to record all backscattered energy from within the beam footprint. We find that 24% of the ice sheet exhibits greater topographic variance within the footprint than can be captured by the range window, and that the window placement captures a median of 90% of the total possible topography that could be recorded. These findings provide a better understanding of the performance of the Sentinel-3 altimeters over ice sheets, and can guide the design and optimisation of future satellite missions such as the Copernicus Polar Ice and Snow Topography Altimeter (CRISTAL).

1 Introduction

From 1992 to 2020, the Antarctic Ice Sheet (AIS) lost a total of 2671 ± 530 billion tonnes of ice (Otosaka et al., 2023), with current rates of ice loss now ∼6 times greater than those measured in 1979 (Rignot et al., 2019). Recent studies suggest that this accelerating loss of ice, which has occurred mostly across sectors of West Antarctica and the Antarctic Peninsula, increased global sea levels by 7.4 ± 1.5 mm from 1992 to 2020 (Otosaka et al., 2023). As Earth's climate continues to warm, current projections suggest that the sea level contribution from the AIS will reach multiple decimetres by 2100, with high-end projections exceeding 1 m (Frederikse et al., 2020). This large range in projections, whilst partly due to a variety of forcing pathways, is also linked to uncertainty in the physical processes governing the ice sheet's response to climate change. Within

25   this context, it is imperative to establish and maintain long-term monitoring programmes to better understand the physical processes that control ongoing ice sheet imbalance (Davis et al., 2005; Price et al., 2011; Shepherd et al., 2004). Whilst a range of techniques exist for remote observation of the cryosphere, our understanding of how ice sheets are changing is largely informed by satellite observations, with the longest continuous record coming from the technique of satellite radar altimetry. The principal use of altimetry over ice sheets is to derive estimates of ice sheet elevation and elevation change (Wingham et al.,

30   1998; Shepherd et al., 2019), which, ultimately, can be used to determine ice sheet mass imbalance. Radar altimeters have also been used to investigate a range of other glaciological processes, including grounding line location and migration (Dawson and Bamber, 2017; Rignot et al., 2011), subglacial hydrology (Siegfried and Fricker, 2018; Siegert et al., 2016), ice shelf processes (Griggs and Bamber, 2011; Chuter and Bamber, 2015), and surface mass balance (Pritchard et al., 2010; Simonsen et al., 2021).

     The initiation of continuous ice sheet monitoring by altimetry began with the launch of the ERS-1 mission in the early 1990s,

35   albeit ERS-1 was designed primarily to measure the ocean geoid. Continuity during the following two decades was provided by the ERS-2 and Envisat satellite missions, before the launch of CryoSat-2 (CS2) in 2010 introduced technical innovations specifically tailored for ice surfaces. Subsequently, Sentinel-3 (S3), which to date comprises two satellites launched in 2016 and 2018, ushered in an era of operational monitoring and global Synthetic Aperture Radar (SAR) coverage, thus representing another significant milestone in the historical progression of satellite altimetry (Abdalla et al., 2021).

40   The measurements made by radar altimeters over the past 30 years have provided important new insight into the changing nature of Earth's ice sheets. However, like all geodetic techniques, the fidelity of measurements varies, as a consequence of both the instrument design and the complexity of the illuminated ice surface. In the case of radar altimeters, measurement quality typically degrades with topographic complexity, due to the difficulty of keeping track of the ice surface, assumptions made within the Level-2 processing, and the limitations imposed by the instrument resolution. Whilst a number of previous

45   studies (Brenner et al., 2007; McMillan et al., 2019; Clerc et al., 2020a; Quartly et al., 2020b; McMillan et al., 2021) have quantified the overall accuracy of elevation measurements derived from the Sentinel-3 altimeter, less attention has been given to investigating the underlying performance of the instrument and, ultimately, how characteristics relating to the instrument and algorithm design have affected the ability of the altimeter to make reliable elevation retrievals. With the recent availability of high resolution Digital Elevation Models, such as the Reference Elevation Model of Antarctica (REMA; (Howat et al., 2019)),

50   comes the opportunity to evaluate a number of these design choices, and therefore to advance our understanding of altimeter performance. This, in turn, can benefit the design and operation of future altimeter missions. In this study, we therefore use REMA to undertake a detailed evaluation of Sentinel-3 elevation retrievals across the Antarctic Ice Sheet, in order to better understand the impact of topographic characteristics on altimeter performance.

2   Principles of Radar Altimetry

55   In this section we briefly review the principles governing the acquisition and processing of radar altimeter echoes over ice sheet surfaces, which provides the context for the analysis presented in this study. Radar altimeters work by transmitting a short radio-wave pulse towards Earth's surface and recording the returned echo in the form of a discretised waveform. Each

recorded waveform, comprising the sum of incident surface reflections from within the altimeter footprint ordered by arrival time (Brown, 1977), encodes information pertaining to the surface illuminated by the satellite, such as topography, electromagnetic scattering characteristics, and in the case of returns over ocean, wind speed and significant wave height (Quartly et al., 2020a). Over uniform surfaces, altimeter waveforms take a distinctive shape, with a clear peak in power, corresponding to the first return from the surface at the point-of-closest-approach (POCA) to the satellite, followed by a gradual decay in the received power.

For echoes acquired over ice sheet surfaces, however, and in particular in regions close to the ice margins, waveform shape can be more complex, due to discrete, equidistant regions of backscatter within the illuminated beam footprint. Nonetheless, from each recorded echo, an estimate of surface elevation can be derived by measuring the range between the satellite and a fixed point on the leading edge of the waveform, which is assumed (in the case of non-interfrometric altimetry) to correspond to the POCA return. This range measurement can then be converted to an estimate of the surface elevation at the POCA, given knowledge of the satellite altitude. In addition, estimates of the ice sheet's backscatter coefficient (sigma-0) can be used to characterise ice sheet properties such as snow depth, grain size, and density (Blarel et al., 2015; Mertikas et al., 2020).

In practice, the retrieval of ice sheet elevation measurements involves a number of onboard and on-ground processing steps, relating to the acquisition and subsequent processing of the altimeter echo. These include (1) surface tracking, (2) retracking, (3) determination of POCA, and (4) geophysical and instrumental corrections, and are described in turn below.

2.1 Surface Tracking

In order to capture the backscattered radar pulse that forms each waveform, the altimeter records the incoming energy for a discrete amount of time, corresponding to when it expects the reflection to be received from the surface. Radar altimeters can have a recording window as low as several microseconds, and when this fails to coincide with the surface return then the instrument temporarily loses track of Earth's surface. Therefore, in order to capture returns effectively, an altimeter requires an estimate of the predicted range to the approaching surface. To provide such information, two methods are utilised: "closed-loop" and "open-loop" tracking. Closed-loop tracking predicts the next range based on the history of the last few seconds. Whilst this works well when the range has linear variation, such as over the ocean or the low slope interiors of the ice sheets, its performance degrades over more highly variable terrain, because the range history is a less reliable predictor of the future range evolution (Quartly et al., 2020b). In contrast, open-loop tracking uses information from an a priori Digital Elevation Model (DEM) to provide the satellite with an estimate of the expected range to the ice surface. This method, first applied onboard the Jason-2 mission, has the potential to more precisely track the complex topography that is found across many parts of the ice sheet margin. However, with the exception of Sentinel-3A's commissioning phase, and isolated ad hoc acquisitions, it remains largely untested to date over ice sheet surfaces (Quartly et al., 2020b; Donlon et al., 2012a).

2.2 Retracking

During Level-2 (L2) processing, the position of the waveform leading edge relative to a specific onboard tracking gate is estimated. This process is known as "retracking". In general, retracking algorithms can be categorised as "physical" or "empirical".

Physical retrackers fit an analytical model to the received waveform in order to represent the underlying physics of the radar wave's interaction with the scattering surface, whereas empirical retrackers solely consider the geometry of the recorded waveform (Villadsen et al., 2016; Passaro et al., 2022). In practice, physical retrackers are rarely used over ice sheets, because they are too sensitive to irregular waveform shapes caused by complex terrain and changes in the scattering properties of the surface

95 (Quartly et al., 2020b). Conversely, empirical retrackers do not assume waveform shape, and as such, are far more robust to cases where the echo deviates from its theoretical shape. Examples of physical retrackers include Ice-2 (Ehlers et al., 2023), applied to low resolution mode ENVISAT data, and SAMOSA (Ray et al., 2015), which has been applied to delay-doppler Cryosat-2 and Sentinel-3 data. Examples of empirical retrackers include TFMRA (Threshold First Maximum Re-tracker Algorithm) (Helm et al., 2014) and a threshold OCOG (Offset Centre of Gravity) (Wingham et al., 1986), the latter of which is

100 deployed in the Sentinel-3 ground segment.

2.3 Determination of the Point of Closest Approach

As the measured range to the POCA is 1-dimensional, it is insufficient to determine the location of POCA in 3-dimensional space; rather it constrains POCA to lie upon an iso-range surface, a constant distance from the satellite. Solving for this ambiguity – to determine the location of POCA – is known as slope-correction, and uncertainties in applying the correction represent

105 a significant source of uncertainty in non-interferometrically derived elevation measurements (Li et al., 2022). Historically, to identify the POCA location, "slope-based" methods were used. These assumed a constant slope within the beam-limited altimeter footprint, which was commonly derived using a priori slope data at nadir (Levinsen et al., 2016; Remy et al., 1989). By assuming an orthogonal reflection from the surface, the approximate location of the POCA can then be determined using trigonometry (Roemer et al., 2007; Brenner et al., 1983). Whilst the assumption of constant slope is reasonable over simpler,

110 homogeneous terrain, the slope method neglects the finer-scale topography within the beam limited footprint, which may lead to inaccuracies over more undulating areas (Levinsen et al., 2016). To address this, "point-based" methods were developed which locate the POCA by using a DEM to search for points with minimum range within the beam-limited satellite footprint. (Li et al., 2022; Roemer et al., 2007; Levinsen et al., 2016). Such an approach was first introduced by Roemer et al. (2007), who found that it outperformed slope-based methods over Lake Vostok within the East Antarctic interior. More specifically,

115 the method moves a fixed window the approximate size of the satellite's pulse-limited footprint through DEM data within the beam-limited footprint (Roemer et al., 2007). The POCA location is then identified as the centroid of the window that minimises the mean range between the satellite and the DEM points within that window, with interpolation between DEM nodes used to further improve accuracy and precision. More recently, a formulation of a point-based method was proposed by Li et al. (2022), which utilised the ranges spanned by the waveform leading edge to identify the DEM points corresponding to the

120 POCA. The POCA, and consequently the slope correction, is then derived from the mean of these points, with this approach also generalisable to allow retrieval of multiple elevations from a single multi-peaked waveform (Huang et al., 2024). These methods, referred to as LEPTA and MPI respectively, were found to outperform other methods in the derivation of ice sheet elevation. More recently still, the AMPLI model was introduced by Aublanc et al. (2024), which further enhances the accuracy of POCA location determination by employing facet-based numerical simulations combined with high-resolution DEM

125   data to simulate Sentinel-3 UnFocused-Synthetic Aperture Radar (UF-SAR) waveforms. This approach was found to reduce
slope-related errors and yield more precise ice sheet elevation measurements than prior methods.

2.4   Geophysical and Instrumental Corrections

Before use, measurements need to be corrected for both geophysical and instrumental factors. These include accounting for the
distance between the antenna and satellite centre of mass, dry and wet troposphere delays, ionospheric delays, and variations in
130   the solid Earth, ocean loading, and polar tide (Quartly et al., 2020b). Additionally, ocean tide and inverse barometer corrections
need to be applied over floating ice such as ice shelves, the latter of which accounts for changes in atmospheric pressure.
Measurements of the satellite range are also impacted by the on-board clock (ultra-stable-oscillator) responsible for measuring
the round-trip of the echo (Quartly et al., 2020b). Approaches for accounting for these various corrections differ from mission
to mission but commonly amount to adjustments of the order of several meters in total. For additional details relating to the
135   corrections applied within the Sentinel-3 ground segment, the reader is referred to (S3-MPC, 2022).

3   The Sentinel-3 Mission

This study focuses upon the performance of the Sentinel-3 radar altimeter. In this section, we therefore introduce the principal
characteristics of the mission.

3.1   Mission and Instrument Overview

140   The EU's Copernicus programme oversaw the design and production of a significant number of new satellites during the 2010s.
One of these missions, Sentinel-3, has so far launched two satellites, the first of which, Sentinel-3A, launched on 6 February
2016, followed by Sentinel-3B on 25 April 2018. Sentinel-3 was designed, in part, as a successor to the European Space
Agency's (ESA) previous altimetry satellites, ERS-1, ERS-2, and Envisat, with the intention of transitioning to an operational
programme, and securing a near-continuous ∼30 year record of global altimetry data. During the lifetimes of Sentinel-3A
145   and 3B, two further satellite launches are planned, Sentinel-3C and D, in order to sustain an unbroken observational record
into the next decade. Sentinel-3 has an orbital period of 101 minutes such that after 385 complete revolutions (27 days), the
ground-track is repeated to within 1 km. This orbital configuration yields an across-track spacing of 0.94 ° longitude at the
Equator (Quartly et al., 2020b). Both the 3A and 3B satellites orbit with a 98.65 ° inclination, thus providing coverage between
81.35°S and 81.35°N. The orbit is also configured to maintain a short-repeat sub-cycle, such that after 4 days the mission
150   obtains quasi-global coverage, with a wider ∼7 ° spacing of ground tracks at the equator (Quartly et al., 2020b). Driven by
its mission objectives, Sentinel-3 operates in a lower inclination orbit and with a much smaller range window than CryoSat-2
(∼92.03 ° and ∼240 m in SAR (Synthetic Aperture Interferometric mode), respectively). The lower inclination orbit means
that significantly more of the interior of the AIS is missed. However, as Sentinel-3 operates in SAR mode across the entire AIS
(unlike CryoSat-2), the interior of the ice sheet is for the first time mapped with a higher along-track resolution. Due to the
155   smaller range-window, it is not uncommon for Sentinel-3 to fail to capture the surface echo, especially across coastal regions

of the ice sheet that exhibit complex topography. Although Sentinel-3 has the capability to operate an open-loop tracker (first introduced on Jason-2) known as the Open-Loop Tracking Command (OLTC), early assessments over the ice sheets' margins that were conducted during the Sentinel-3A commissioning phase led to the decision to favour closed-loop tracking over the ice sheets (Quartly et al., 2020b).

160   The primary altimetry instrument on board Sentinel-3, SRAL (Synthetic Aperture Radar Altimeter), is a Ku-band SAR altimeter, which provides measurements with a resolution of ∼300 m along-track by ∼1.6-2 km across-track, depending upon surface topography (Quartly et al., 2020b). The use of unfocused Synthetic Aperture Radar (SAR; also referred to as Delay-Doppler) processing (Love, 1985), allows the motion of the satellite relative to Earth's surface to be exploited, to deliver a four-fold improvement in the along-track resolution compared to traditional low resolution altimeters which are pulse-limited

165   along track. Specifically, SRAL emits patterns of 64 coherent Ku-band pulses in a burst (i.e. with a high Pulse Repetition Frequency of 17.825 kHz), surrounded by 2 C-Band pulses (Donlon et al., 2012b). A fast Fourier transform is then applied to the returned echoes in order to partition the received power into 64 "Doppler strips" along-track, and thus increase the instrument resolution to ∼300 m along-track. Moreover, as a given Doppler strip is seen in the radar footprint multiple times, different looks of the same Doppler strip can be "stacked" in order to reduce the impact of radar speckle; a process that is

170   referred to as multi-looking. While the concept of SAR processing has been applied within the context of radar imagers since the 1950s (Love, 1985) and has seen extensive application in previous satellite missions (Curlander and McDonough, 1991; Kovaly, 1976; Rosen et al., 2000), SAR processing has only recently been utilised by Earth-orbiting altimeters with the launch of CryoSat-2. This innovation has represented an important advance in polar Earth Observation, allowing smaller-scale features across ice sheets and sea ice to be resolved (Raney, 1998; Tilling et al., 2015). Accompanying SRAL, Sentinel-3 also carries

175   a microwave radiometer (MWR), Sea and Land Surface Temperature Radiometer (SLSTR) and an Ocean and Land Colour Imager (OLCI) (Clerc et al., 2020b).

4   Data

The objective of this study is to provide a detailed assessment of the impact of surface topography on the performance of SRAL across the AIS. For the purposes of this study, we therefore analysed one complete cycle of data acquired by both

180   Sentinel-3A and Sentinel-3B. Specifically, we selected cycle 54 for S3A and cycle 35 for S3B, which were acquired over the periods 15th January to 11th February 2020 and 25th January to 22nd February 2020, respectively. We used the enhanced, baseline 4, non-time-critical, S2_2_LAN___ product, which was downloaded from the Copernicus Open Access Hub (https://scihub.copernicus.eu/dhus/#/home), and represented the latest product release at the time of the study.

    In order to investigate the performance of Sentinel-3, we used the 100 m resolution, version-2 REMA (Reference Elevation

185   Model of Antarctica) mosaic (Howat et al., 2018). REMA is a high-resolution DEM covering nearly 98% of Antarctica, which has been used for a range of cryospheric applications (Chartrand and Howat, 2020; Zinck et al., 2023; Liu et al., 2023). REMA was created by applying stereophotogrammetric techniques to submeter resolution commercial optical satellite imagery, including data from Maxar, WorldView-1, WorldView-2, and WorldView-3, as well as a small number of acquisitions made by

GeoEye-1 (Howat et al., 2019). To form the mosaiced product, individual DEMs were registered to satellite altimetry measure-
ments from CryoSat-2 and ICESat, leading to an estimated absolute uncertainty of less than 1 m, and relative uncertainties of
the order of decimeters (Howat et al., 2019). In order to improve computational efficiency when performing assessments at the
ice sheet scale, we resampled the 100 m REMA mosaic to 200 m using nearest-neighbour interpolation.

5   Methodology

In this study, our aim is to assess and better understand the performance of the S3 altimeter over a variety of topographic
regimes. To achieve this, we firstly use REMA to generate new ice sheet wide estimates of surface slope and roughness. We
then performed three different sets of analysis (1) an assessment of the extent to which the placement of the S3 range window
successfully captures the point of closest approach on the illuminated ice surface, (2) an evaluation of the extent to which the
onboard tracker's placement of the range window and subsequent L1 processing maximises the proportion of the illuminated
topography that contributes to each waveform, and (3) quantification of the degree of correlation between along-track sequences
of echoes. The first analysis is designed to evaluate the assumption – which is inherent to most L2 processing schemes – that
the waveform leading edge originates from the closest point within the beam footprint; and then to investigate how the validity
of this assumption varies with increasing topographic complexity. The second analysis is designed to provide a first assessment
of the effectiveness of the altimeter in adequately tracking the underlying topographic surface. The third analysis evaluates the
extent to which the complexity of the topographic surface – characterised by slope and roughness – causes decorrelation in
successive delay-Doppler echoes. In the following sections, we outline the methodology used for each of these analyses, in
turn.

5.1   Ice Sheet Surface Slope and Roughness from REMA

To understand the impact of ice sheet surface topography on the performance of the Sentinel-3 altimeter, we used the REMA
dataset to compute continent-wide estimates of ice sheet surface slope and roughness. Within the context of this study, these
parameters are important because they can affect (1) the ability of the altimeter to track the ice sheet surface, (2) the effective-
ness of approaches to derive the Level-1b (L1b) waveform, and (3) the degree of correlation between sequences of waveforms
acquired along the satellite track.

We generated our own slope and roughness maps using REMA in order to tailor the algorithms used to fit with the objectives
of this study. Although there exist several easy-to-apply methodologies for calculating slope from DEMs (Horn and Schunck,
1981; Zevenbergen and Thorne, 1987), common approaches for calculating roughness such as the Terrain Ruggedness Index
(TRI) (Riley et al., 1999) and the Topographic Position Index (TPI) (Wilson et al., 2007) do not fit our use-case, despite
extensive application in GIS (Geographic Information System) programs and packages such as GRASS, ArcGIS, and GDAL
(used by QGIS). This is because these methods use the local variance in elevation as a measure of roughness, but neglect to
account for topographic slope. Instead, they calculate the differences between a pixel and its immediate neighbours, which
would, for example, return a non-zero roughness value over a perfectly smooth plane inclined at an angle. As such, values

determined for slope and roughness calculated in this way encode each other via complex, non-linear interactions. To address this, we therefore calculate roughness independently of slope, by taking the dispersion of orthogonal residuals from a plane fitted through a given DEM point and its neighbours. To do so, we use Singular Value Decomposition (SVD), which we apply using a sliding-window approach. Specifically, we use a 5x5 pixel (1000x1000 m) window, with slope and roughness

225   parameters only computed where more than half of the pixels within a window contained a valid elevation measurement. The window size was chosen to be broadly consistent with the size of the pulse limited footprint and to minimise the impact of missing data. To obtain slope and roughness values, we first centre the data within each window by subtracting the means of their x, y and z coordinates. We then apply SVD in order to decompose the centre points in each window into three distinct matrices (Equation 1), and take the left singular matrix, U, which contains three orthogonal unit vectors describing a plane of

230   best fit:

$$M = U\Sigma V^T \tag{1}$$

Here, $\mathbf{M}$ the is original matrix that we want to decompose, $\mathbf{U}$ is the left singular matrix, $\mathbf{\Sigma}$ is a diagonal matrix containing singular eigenvalues, $\mathbf{V}$ is the right singular matrix, and T is the matrix transpose operator.

By calculating the partial derivatives $\frac{dz}{dx}$ and $\frac{dz}{dy}$, we determine the resulting gradient and hence the surface slope. Roughness

235   is then directly computed based on the standard deviation of the orthogonal residuals, which are calculated by taking the dot product of the centred elevation points with the normal vector to the plane. Since we define roughness to be one standard deviation of the orthogonal residuals, it is important to note that the values stated in the text should be interpreted as characterising 68% of the roughness variance, and not the peak-to-trough elevation difference, or amplitude, of the local topographic variation.

240   ## 5.2   Window Placement Optimisation

Prior to performing a detailed assessment of the range window placement relative to the point of closest approach (Sect. 5.3), we first investigated more broadly the extent to which the placement of the range window maximises the capture of the topographic surface illuminated by the beam footprint. Specifically, for each echo within our chosen cycles (comprising a total of 8,124,014 records), we computed the proportion of DEM points within the beam footprint that fell above, within and below

245   the ~60 m range window, where the beam footprint was defined with dimensions of 18,200 and 300 m in the across and along-track directions, respectively.

Because over complex topography, the range of elevations within the beam footprint exceeds that spanned by the range window, it is, in places, impossible for the range window to entirely capture the illuminated topographic surface. To account for this, we therefore also compute the positioning of the range window that maximises the capture of topography, together

250   with the associated percentage of the illuminated surface that could be captured within it. This is done by iteratively moving the range window by 1-meter increments in range, to determine the position that maximises topographic capture. Having located the optimal range window location, we then quantify the possible increase in the proportion of the surface captured, which

could be realised with a refined range window placement. This is computed as the ratio of actual to maximal topographic capture.

5.3 Capture of the Point of Closest Approach

Following the methodology presented in Sect. 5.1, we also perform a similar assessment, which is focused specifically on the window position relative to the point of closest approach. This is motivated by the fact that, within conventional L2 altimetry processing chains, an assumption is made that the echoing point (the so-called POCA) lies within the intersection of the range window and the beam limited footprint (class 2 in Fig. 1). However, around the complex topography of the ice sheet margin, this assumption does not always hold, particularly for Sentinel-3, due to its small (∼60 m) range window. In regions of high slope, the POCA may lie outside the beam limited footprint, meaning that any backscattered energy will be highly attenuated by the antenna gain pattern, whereas in regions of rugged (highly variable) topography, the POCA may lie at an elevation not captured by the range window. With the availability of new, high-resolution DEMs such as REMA, comes the opportunity to explicitly assess the extent to which the echoing point lies within the intersection of the beam limited footprint and the range window, and hence the extent to which this common assumption in L2 processing chains is satisfied. Furthermore, by comparing success and failure at the ice sheet scale to covariates such as surface roughness and slope, it is possible to assess how performance is affected by topographic complexity. For all S3A and S3B echoes within our chosen cycles, we therefore classified where the identified POCA location lay relative to the positioning of the S3 range window. The acquisition geometry and related definition of the POCA classes are shown in Fig. 1.

Within this assessment, we performed two sets of analyses. First, we evaluated the positioning of the range window relative to the POCA location that was defined within the standard L2 product. This allowed us to determine the extent to which the slope correction applied within the L2 processing chain identified an echoing point that was consistent with the actual acquisition geometry (i.e. lay within both the beam footprint and range window). Secondly, we performed the same evaluation, but for a POCA location that we determined, independently, by minimising the range between the ice surface and the altimeter, using the REMA DEM. This is analogous to the relocation approach of Roemer et al. (2007), albeit we extend the search region to include instances where the POCA lies beyond the 3dB beamwidth (Fig. 1). As such, we refer to this as the Roemer-derived POCA. This analysis is designed to evaluate the extent to which the POCA is actually captured within the 3-D window defined by the range window and the antenna 3dB beamwidth.

To perform these analyses, we first located the range window relative to the ice surface for each of the ∼8 million altimeter records, and then compared it to the two POCA locations. Specifically, we adjusted the range to the nominal tracking point (defined for S3 as the 43rd bin in the range window) according to the geophysical and instrument corrections supplied within the product, to account for path delays due to dry tropospheric, wet tropospheric and ionospheric effects; tidal and atmospheric pressure induced variations, and the instrument Centre of Gravity (COG) correction. As all of these corrections are supplied at 1 Hz, we used linear interpolation to match these to the native 20 Hz frequency of the range and elevation measurements. Finally, the dimension of the range window (128 bins) was used to locate the range to the start and end of the window for each record. To reference the range window to the DEM elevation, we then subtracted the satellite altitude.
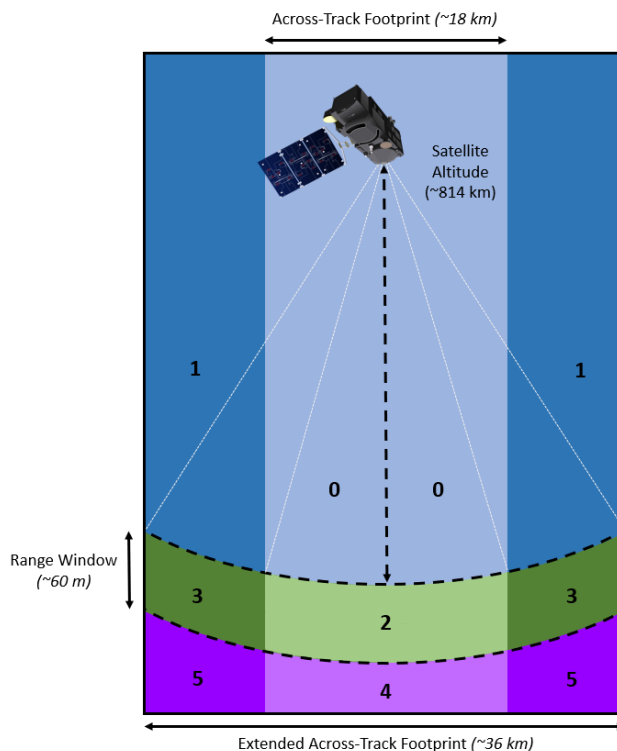
Figure 1. Illustration of the Sentinel-3 SAR altimetry acquisition geometry in the across-track plane (satellite flying into the page), showing the classification scheme used to categorise each echo according to the location of the POCA relative to the positioning of the L1b range window. Above the range window is shaded in blue (classes 0, 1), below in magenta (classes 3, 4), and within the range window in green (classes 2, 3). Darker shades of each colour represent locations outside of the across-track beamwidth.

Next, we computed the geographic coordinates and elevation of the POCA for both the L2 and Roemer derivations, in order to classify them according to their position relative to the range window (Fig. 1). For the L2 evaluation, the geographic coordinates (x,y) were simply taken from the product. For the surface elevation (z) at the L2 POCA, we chose to extract the elevation at this location from the closest REMA pixel, rather than use the elevation within the altimeter product, because the purpose was simply to compare the range window to a reference surface, rather than interpret the altimeter elevation itself. This approach therefore avoided missing data in the L2 product. We chose the closest REMA point, rather than employing interpolation, as the DEM posting of 200 m is smaller than the resolution of the altimeter measurements ($\sim$1600 x 300 m). For the Roemer derivation of the POCA, we computed the echoing point location based upon the pixel that minimised the range between the satellite and the ice surface.

5.4 Along-track Decorrelation of Echoes

Finally, we explored the extent to which ice sheet surface topography causes decorrelation in sequences of SAR waveforms, as they are acquired along the satellite track. This analysis extends the work of McMillan et al. (2019), to investigate the rate at which waveforms decorrelate in space (along-track), and the extent to which this is governed by the topographic characteristics

300 (slope and roughness) of the surface. More specifically, we calculated (1) correlations between adjacent pairs of waveforms aligned in range, and (2) correlations between a seed waveform and its subsequent 50 records (spanning a distance of ~15 km), also aligned in range. The latter assessment allowed us to quantify the rate at which waveforms decorrelate in space, spanning distances that are representative of those over which altimetry measurements are commonly aggregated, for example when computing rates of surface elevation change.

305 To do this, we first normalise each waveform and reject any waveform whose mean power does not exceed the estimated thermal noise by more than 0.15, with thermal noise computed as the mean of the 6 lowest-value waveform samples (Helm et al., 2014; McMillan et al., 2019). To compute the correlation of any given waveform pair, we first align both waveforms according to their centres of gravity (COG) (Equation 2), removing any bins that lie beyond the bounds of the original waveform samples. In order to focus on correlating the principal surface response, rather than waveform noise, we mask the aligned

310 waveforms by removing peripheral bins from each side of the range window, until a bin with power above 0.15 (chosen for consistency with previous noise detection and visual inspection) is found in either waveform. If the clipped waveforms have at least 16 bins remaining, we then compute the Pearson correlation coefficient using the pairs of normalised waveform samples. A minimum threshold of 16 bins was chosen as a reasonable lower bound for what constitutes a valid response based upon an assessment of the waveforms that passed the L2 ice quality checks, which retained a mean COG width of 27.1 bins and

315 standard deviation of 10.2.

$$COG = \frac{\sum_{n=1}^{N} n P_n^2}{\sum_{n=1}^{N} P_n^2} \tag{2}$$

Here, N is the number of waveform bins (128), and P_n is the power at bin n.

We repeat this process for each of the subsequent 50 waveforms in the sequence, in order to derive a series of correlation values relative to the seed waveform. Then, where more than 25 correlation values are returned, we fit a linear regression to

320 estimate the rate of change in correlation as a function of distance along-track. We constrain the regression to be 1 at its initial value, and then, using the correlation gradient, compute the change in the correlation coefficient at record 50. This provides a more stable estimate of the change in waveform correlation after 15 km, which is not solely dependent upon the initial and 50th records. Based on this approach, a value of 0 indictates that waveforms 15 km away are perfectly correlated, whilst a value of -1 corresponds to waveforms that are fully decorrelated (R=0) after 15 km. Values less than -1 indicate that waveforms are

325 anti-correlated after 15 km; i.e. an increase in power in one waveform corresponds to a decrease in power in the other. This is likely to reflect limitations in the COG alignment of complex waveforms (e.g. correlating a single peak with a double peak waveform) and so we focus our analysis on correlation values between 1 and 0.
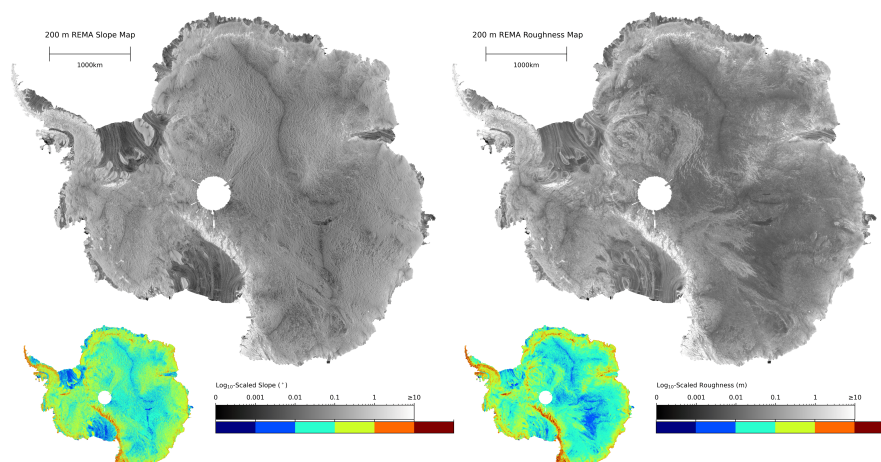
Figure 2. 5 km resolution, $\log_{10}$-scaled slope and roughness maps of Antarctica generated using 200 m resolution REMA and the Singular Value Decomposition techniques outlined in Sect. 5.1. The coloured inset maps show discretely binned versions of these datasets, to aid the visualisation of broader scale patterns.

6 Results

6.1 Ice Sheet Slope and Roughness from REMA

330   First, we analysed the surface slope and roughness characteristics of the Antarctic Ice Sheet, based upon our newly-derived REMA datasets (Fig. 2). Our new surface slope map shows well-established patterns of very low (< 0.03 °) surface slope at the ice divides and the floating ice shelves, with steeper slopes prevailing towards the grounded ice sheet margin. Overall, we find that 57.4% and 90.1% of the ice sheet have a surface slope below 0.1 and 0.5 °, respectively. In addition to the large-scale characteristics of slope, our new map also shows detailed signatures of topography and ice dynamics, such as the flow of ice
335   across the Ross and Filchner-Ronne Ice Shelves from their upstream tributaries, and the numerous ice rises that lie close to these ice shelves' grounding lines. Turning to ice sheet surface roughness, we find that that 64.9% and 89.5% of the ice sheet have a 1-standard deviation surface roughness below 0.1 and 0.5 m, respectively, with lower roughness persisting mostly within the interior of the ice sheet. Of particular note are the clear signatures of mega dune fields in East Antarctica, which typically have roughness of the order of ~1 m and the patterns associated with ice flow across the Ross and Filchner-Ronne Ice Shelves.
340   In broad terms, the interior of West Antarctica is rougher than East Antarctica and, as with surface slope, there is a general trend to increasing roughness towards the ice margin, with surface roughness often reaching several meters close to the coast.

We find that the ice sheet as a whole has a median slope and roughness of 0.070 ° and of 0.061 m, respectively. We characterise the degree of spatial variability of each parameter across the ice sheet by computing the median absolute deviation, which is 0.044 ° and 0.045 m for slope and roughness, respectively. To explore in more detail the relationship between surface
345   slope and roughness, we plot their joint and marginal distributions (Fig. 3), which shows a positive relationship between the two
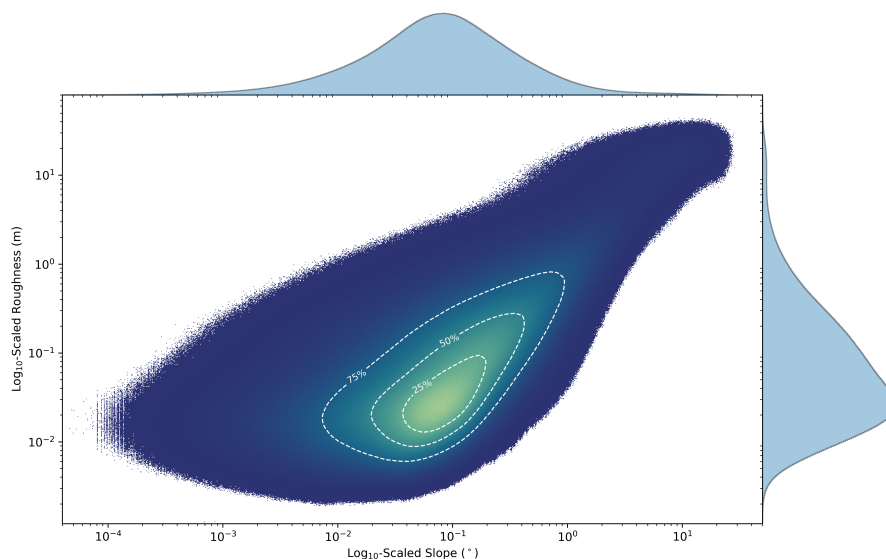
Figure 3. Log$_{10}$-binned joint and marginal distributions of slope and roughness across Antarctica. The joint distribution is displayed as a density plot, with lighter colours indicating a higher density of measurements, and the contours bounding 25%, 50%, and 75% of the data.

variables. Taking the Pearson correlation coefficient, we obtain a value of 0.730 (p-value < 0.01), indicating that the two values are significantly linearly correlated. Because we have calculated roughness via the dispersion of orthogonal residuals to the fitted slope, the two variables remain algorithmically independent. Therefore, this correlation reflects a physical relationship between these topographic glaciological parameters, indicating that areas with higher surface slope are also more likely to exhibit higher surface roughness. Broadly, we find that roughness increases by ∼1.4 m per degree increase in slope.

6.2 Window Placement Optimisation

The S3 L1b product records backscattered energy over a range window of ∼60 m. As such, there are areas of the AIS where the degree of topographic variance within the beam footprint makes capturing the full topography within the range window impossible. Determining the locations and extent of these regions is of interest because it indicates where (1) waveforms are likely to be truncated or highly complex, (2) relocation errors may be prevalent, and (3) positioning of the range window will, ultimately, have a major impact upon reliable retrievals of ice sheet elevation. We found that, for 23.7% of recorded echoes, full topographic capture was impossible within the 60 m range window, with this occurring primarily in coastal areas that exhibit high topographic complexity (Fig. 4 a).

To assess the performance of the current L1b window placement, we then computed the ratio of actual to maximal topographic capture for each record (Fig. 4 b), where the latter was determined by calculating the maximum percentage of the illuminated surface that could have been captured with a refined placement of the range window (Sect. 5.2). On average, the current window placement acquired a median 89.7% of the total possible topography that could be captured, with a median
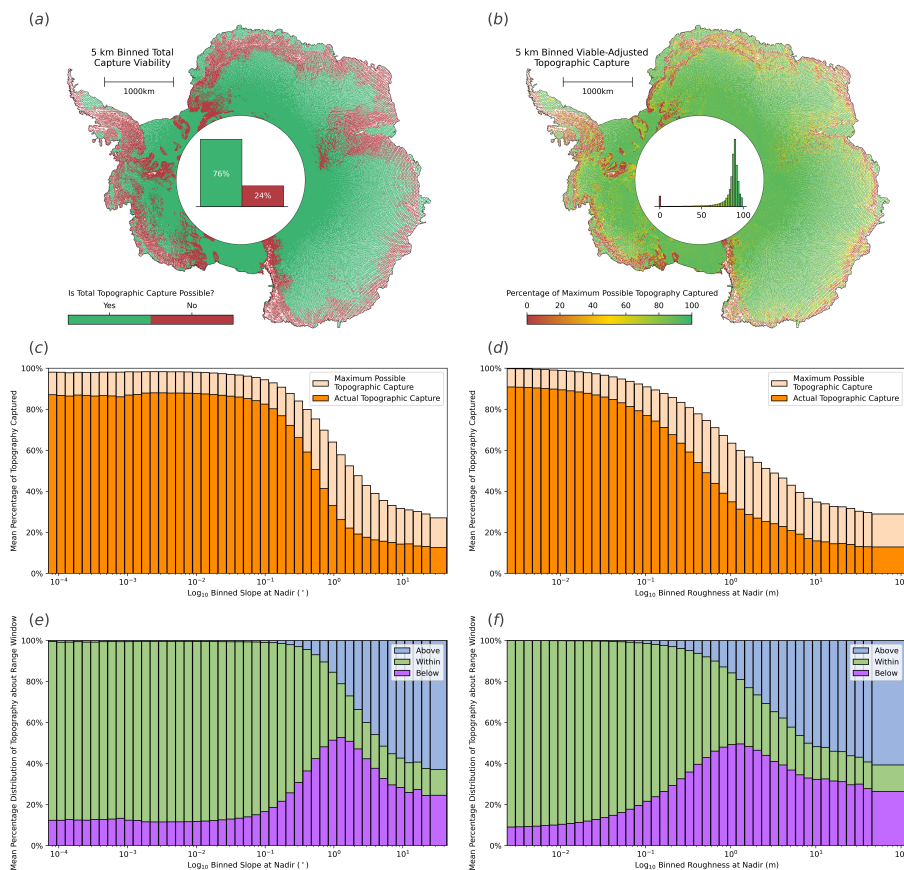
Figure 4. Assessment of the ability of the Sentinel-3 L1b range window to capture the full topographic surface within the beam footprint. Panel a exhibits where total topographic capture within the 60 m range window is possible, binned to 5 km. The percentage of records where full topographic capture is, and is not, possible is shown within the bar graph in the pole hole. Panel b shows the percentage of the maximum possible topography that is captured by the current placement of the range window, binned to 5 km, with the corresponding distribution shown within the pole hole. A value of 0 indicates that the range window entirely misses the ice surface, whereas a value of 100 indicates that the range window captures the maximum possible area of the illuminated surface. Panels c and d show stacked bar charts representing the maximum percentage of topography within the satellite footprint that can be captured, and that which is currently captured, with respect to $\log_{10}$-binned slope and roughness respectively. Panels e and f show stacked bar charts, indicating the distribution of REMA nodes within the illuminated beam footprint that are above, within, and below the range window, with respect to $\log_{10}$-binned slope and roughness.

absolute deviation of 3.27%. This demonstrates that, even over areas where full topographic capture is impossible, further refinement to the placement of the range window could allow a larger proportion of the surface return to be recorded. Notably, in 2.20% of cases, the high topographic variability within the illuminated footprint meant that positioning the range window to maximise topographic capture resulted in the return from the POCA being missed. In these cases, there is a trade-off between maximising topographic capture and acquiring the reflection from the point of closest approach. For future missions that aim

for full waveform retrievals, (such as swath processing), this type of analysis can help to inform decisions relating both to the size (range dimensions) and the positioning (onboard tracking) of the range window. It should also be noted that it is important to resolve an unambiguous leading edge, which requires a short period of no backscattered power to be recorded prior to the first return.

Comparing these results to our new slope and roughness datasets, we find that both the actual, and theoretical maximum, percentage of the illuminated topography that can be captured within the S3 range window decreases with increasing slope and roughness (Figs. 4 c and d). Specifically, for $\log_{10}$-binned slope we observe a reverse-sigmoidal trend, with ~90% of the illuminated surface typically captured for slopes up to ~0.1 °, followed by a relatively rapid decline to ~10-20% capture by the time slopes reach ~1 °. We see a similar trend in relation to $\log_{10}$-binned surface roughness, with capture rates decreasing with increasing roughness, from ~90% (low roughness) to ~10-20% (once roughness exceeds ~5 m). In both cases, we observe a difference of ~10-20% between the maximum possible percentage of topography captured and the actual captured. These discrepancies are slightly larger within the range of rapid capture decline for both slope (~0.1-1 °) and roughness (~0.01-10 m).

Next, we assessed the mean proportion of the illuminated surface that was above, within, and below the range window. This allowed us to determine the degree to which the window was centered on the target surface, and how this varies as a function of slope and roughness (Figs. 4 e and f). This analysis indicates that the ~10% of the illuminated topography not captured within the range window at lower values of slope and roughness fall predominantly above the range window. As slope and roughness increases, topographic capture decreases, due to the proportion of topography above and below the range window increasing in approximately equal measures. Once slope and roughness exceed ~1.3 ° and ~3 m respectively, the proportion of topography below the range window begins to decrease, and is replaced with surface topography above the range window.

Finally, we evaluated whether the heading of the satellite as it crosses the Antarctic coast has a significant impact on window placement. We found that 50.5% of records within 30 km of the coast were acquired in a configuration where the satellite was flying from land to ocean, and 49.5% from ocean to land. When the satellite is heading from land to ocean, we obtain a median topographic capture (with respect to the theoretical maximum) of 82.7% for records within 30 km of the coast. Conversely, when the satellite flies from ocean to land, we obtain a median topographic capture of 83.5%. With a difference of less than 1%, we conclude that there is therefore insufficient evidence to suggest that coastal heading has a significant impact on window placement.

6.3 Capture of the Point of Closest Approach

Next, we analysed the effectiveness of the positioning of the Sentinel-3 L1b range window in capturing the POCA on the ice surface. In order to explore how performance varied spatially, we binned the L2 POCA classes (LPCs), and the Roemer-derived POCA classes (RPCs) to 5 km, taking the modal values within each grid cell (Figs. 5 B and 6 b). Using our new slope and roughness derivations (Fig. 2), we also explored the relationships between these window placement classes and the topographic parameters.
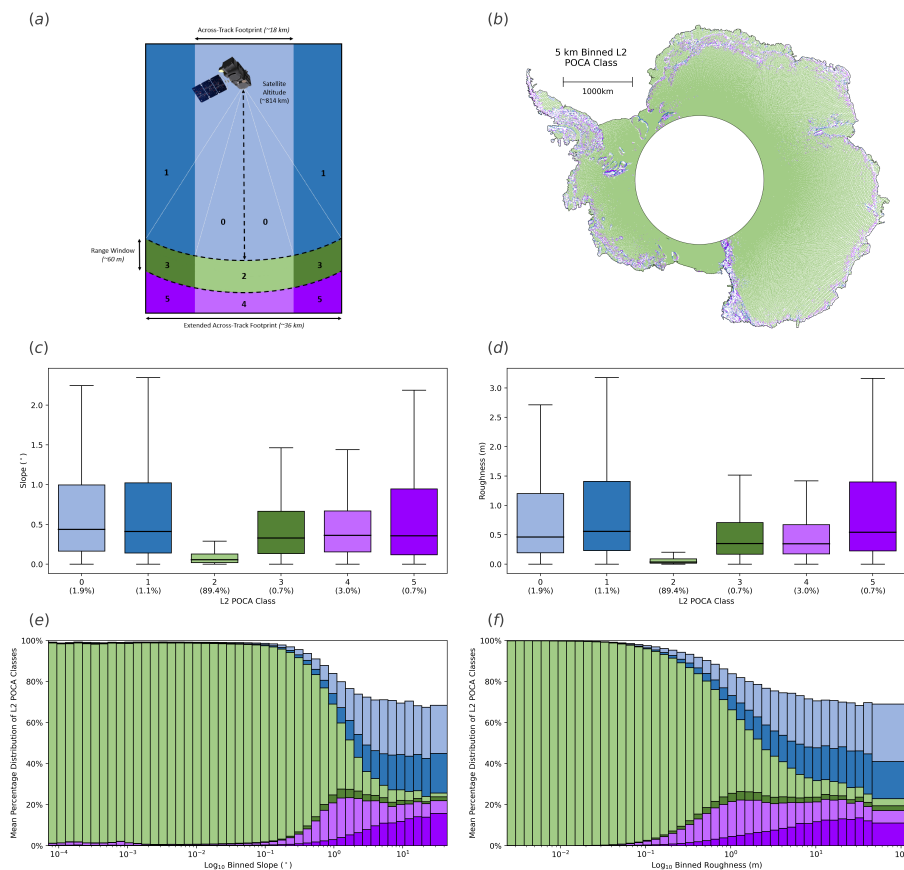
Figure 5. Assessment of the ability of Sentinel-3 to capture the surface reflection at the L2-derived POCA. Panel a outlines the POCA class definitions as per Fig. 1 for ease of cross-referencing. Panel b shows the L2-derived POCA classes, spatially binned to 5 km. Panels c and d show box plots of the L2-derived POCA per-class distribution with respect to slope and roughness, with the percentage of data within each class given in parentheses. Panels e and f show stacked bar charts representing the percentage distribution of the L2-derived POCA classes within each slope and roughness bin.

As a result of quality control and filtering in the L2 processing, we observe that ∼3.19% of the data is missing for the LPCs. The proportion of this missing data increases with slope and roughness, comprising upwards of ∼30% of samples in regions of very high slope and roughness (Figs. 5 e and f, respectively). For 89.4% of the full, non-aggregated data, we observe that the L2 POCA lies within both the Sentinel-3 beam footprint and the L1b range window. This occurs almost exclusively at values of low slope and roughness, with a median of 0.0553 ° and 0.0355 m, and median absolute deviation of 0.0428 ° and 0.0243 m respectively (Figs. 5 c and d). In contrast, the other classes encompass a far greater range of values, retaining significantly higher medians. This is evident spatially, with LPCs with a value other than 2 grouped around areas of complex topography such as the Transantarctic mountains, the Antarctic Peninsula, and coastal regions (Fig. 5 b).

We find that the proportion of L2 POCA falling within both the beam footprint and the range window (class 2) decreases with increasing slope and roughness. For both covariates, the relationship follows an approximate reverse-sigmoidal trend (Figs. 5 e and f), much like the trends found for topographic capture in Sect. 6.2. This suggests that for slope (roughness) values of up to ∼0.1 ° (m), window placement achieves near to 100% capture of the POCA location. As slope increases beyond this limit, however, performance degrades, such that by ∼1 ° only ∼45% of the L2 POCA's lie within the desired range, and by ∼5° this reduces further to ∼5-10% (Figs. 5 e and f). Likewise for roughness, we observe an incremental reduction in performance up until ∼10 m, at which point the proportion of points falling within class 2 stabilises at ∼5-10% (Figs. 5 e and f). With increasing slope and roughness, the observed reductions in class 2 are replaced in approximately equal parts by the other classes, with slightly more cases of classes 0 and 1 (POCA above the range window) than 4 and 5 (POCA below the range window). While classes 0 and 1 increase at similar proportions, class 4 initially outweighs class 5, before class 5 begins to gradually dominate at extreme values of slope and roughness.

The RPCs, which are defined using the location that minimises the range between the surface and satellite, follow broadly the same distribution as the LPCs, with the exception of minimal data loss (∼0.003%), which is due to missing data within the REMA dataset (Fig. 6 b). Similarly to the LPC's, 89.0% of the full, non-aggregated data has an RPC of 2 (POCA within both the beam footprint and range window), with median slope and roughness for this class of 0.0553 ° and 0.0353 m, respectfully (Figs. 6 c and d). In comparison to the LPC's, the RPCs return more cases where the POCA is located above the range window, and less instances where the POCA is below the range window (Figs. 6 c and d). This is unsurprising given that the RPC approach, by minimising the range, favours the highest point within the footprint, which is more often above rather than below the range window. The RPC's exhibit very similar reverse-sigmoidal trends in class 2 as the LPC's, with the proportion of classes 0 and 1 also increasing with slope and roughness in approximate equal parts. However, unlike the LPC's, classes 4 and 5 (POCA below the range window) experience only a temporary increase with increasing slope and roughness, peaking in the range ∼1-10 meters and degrees, respectfully, before being replaced by classes 0 and 1 (POCA above the range window) for more extreme topographic variance (Figs. 6 e and f). We also found that classes 4 and 5 often occur at the transition between floating and grounded ice (Fig. 6 b), where there is a rapid change in the surface gradient, and hence may be due to the inertia in the closed-loop tracker, which positions the range window based upon preceding tracker information. As slope and roughness increase further, then classes 0 and 1 again dominate, reflecting the behaviour typical of mountainous terrain where local topographic highs exceed the positioning of the range window.

Lastly, we again assessed whether the per-class distribution close to the ice sheet coast was affected by the satellite heading for records within 30 km of the coast. For the RPCs, we observed that the range window was adequately placed (i.e. class 2) for 44.9% of the measurements that were acquired when heading from land to ocean, and 45.4% when heading from ocean to land. A difference of only ∼0.5% suggests that again there is insufficient evidence that coastal heading affects the per-class distribution close to the ice sheet coast, agreeing with the negligible difference in topographic capture rate (with respect to the theoretical maximum) observed with respect to coastal heading (Sect. 6.2).
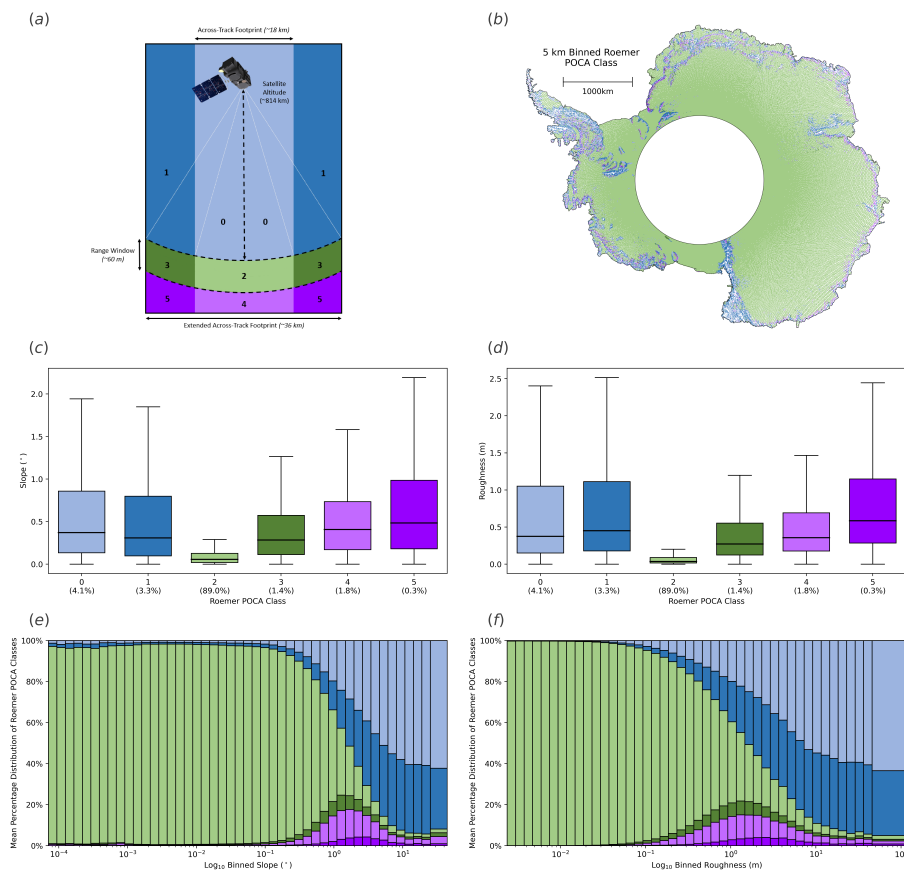
Figure 6. Assessment of the ability of Sentinel-3 to capture the surface reflection at the Roemer-derived POCA. Panel a outlines the POCA class definitions as per Fig. 1 for ease of cross-referencing. Panel b shows the Roemer-derived POCA classes, spatially binned to 5 km. Panels c and d show box plots of the Roemer-derived POCA classes with respect to slope and roughness. Panels e and f show stacked bar charts representing the percentage distribution of the Roemer-derived POCA classes with respect to $\log_{10}$-binned slope and roughness.

6.4 Along-track Correlation of Echoes

Our final set of analyses focuses on exploiting our new slope and roughness datasets to assess the correlation of series of altimetry echoes acquired along the orbit track, with a view to investigating the impact of surface topography on the degree of waveform correlation achieved. To investigate correlation across the entire ice sheet, we bin both the correlation between consecutive waveforms, and the fitted 50-record correlation change, taking the mean values within each 5x5 km grid cell (Figs. 7 a and b). For the inter-record correlation, we found a median of 0.945 and a median absolute deviation of 0.0284, with the distribution skewed towards higher correlation values, and lower values grouped around areas of topographic complexity (Fig. 7 a). For the fitted 50-record correlation change, we found a median reduction in the correlation of -0.419 over 15 km and a median absolute deviation of 0.0258. 4.71% of records had a correlation change of less than -1 and were removed from our
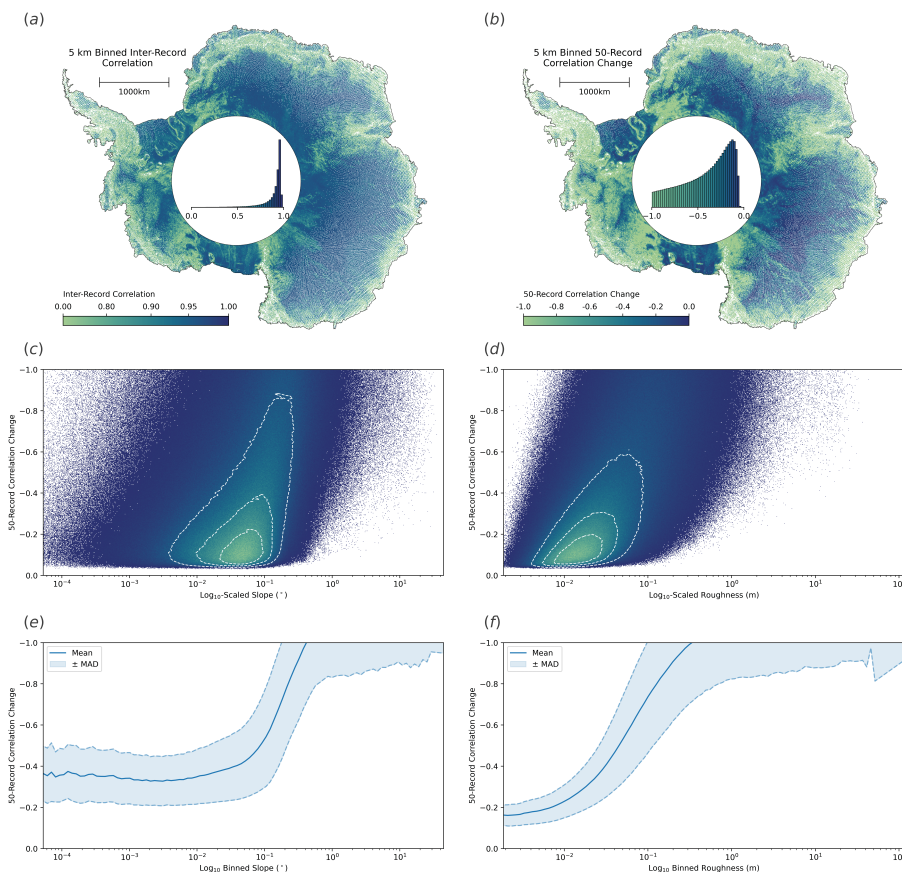
Figure 7. Analysis of the along-track correlation of Sentinel-3 SAR altimetry echoes. Panel a shows the correlation between consecutive records, spatially binned to 5 km. Panel b shows the 50-record correlation change, also spatially binned to 5 km. Histograms showing the overall distribution of each parameter are given within the pole holes of the respective plots. Panel c and d show density plots of the 50-record correlation change as a function of $\log_{10}$-binned slope and roughness respectively. Concentric contours are included, which contain 75%, 50%, and 25% of the data from outside to in respectively. Panels e and f show the mean and median absolute deviation of the 50-record correlation change with respect to $\log_{10}$-binned slope and roughness, respectively.

analysis (as discussed in Sect. 5.4). By comparing qualitatively to our REMA-derived estimates of surface slope and roughness (Fig. 2), it is clear that both of these topographic parameters influence the degree of correlation between waveforms. For example, correlation reduces in areas of high roughness, such as megadune fields in East Antarctica, and high surface slope, such as the coastal margin of the ice sheet (Figs. 7 a and b).

455   Comparing the fitted 50-record correlation change to surface slope and roughness, we see that the 15 km change in correlation remains relatively stable at ∼-0.35, for slopes up to ∼0.01, before dropping rapidly to -1 for slopes above this value (Fig. 2 e). For low surface roughness, the 50-record correlation change is ∼-0.15, but this quickly drops to -1 once roughness ex-

ceeds ~-0.2 m (Fig. 2 f). Taking the Pearson correlation coefficient of the 50-record correlation change to $\log_{10}$-binned surface slope and roughness we find values of -0.534 (p-value < 0.01) and -0.342 (p-value of 0.0199). This implies that, linearly, slope

460 and roughness explain 28.5% and 11.7% of the ice-sheet wide variance in along-track waveform decorrelation. We therefore conclude that, at the 5% significance level, 50-record correlation change is moderately, linearly correlated to $\log_{10}$-binned surface slope and $\log_{10}$-binned roughness, with slope providing a stronger control. Whilst conceptually, it is understood that slope and roughness impact the shape of the echo, and associated parameters such as the number of peaks, leading edge width, and trailing edge slope, this analysis demonstrates quantitatively the strength of this correlation, through the comparison of

465 independent altimetry and DEM-derived datasets.

7 Conclusions

Since the launch of Sentinel-3A in 2016, and Sentinel-3B in 2018, the Sentinel-3 mission has acquired hundreds of millions of echoes over Antarctica, providing topographic information at resolutions of ~300 m along-track by ~1.6-2 km across-track, which are repeated every ~27 days. To date, previous assessments of Sentinel-3 performance over ice sheets have concentrated

470 predominantly on the outputs of L2 processors, namely the high-level validation of the resulting elevation products. Here, we extend previous work by using novel topographic datasets derived from REMA, to more directly explore the underlying factors that influence Sentinel-3's performance. Specifically, we use singular value decomposition to robustly separate local elevation variability into slope and roughness components, and investigate the impact of each upon Sentinel-3 altimeter performance.

Quantitatively, our new estimates of slope and roughness indicate a strong positive correlation (Pearson correlation coeffi-

475 cient of 0.730) between these two variables; areas with higher surface slopes also exhibit greater kilometre-scale (orthogonal) surface roughness. Overall, we find that 57.4% and 90.1% of the ice sheet exhibited slopes below 0.1 and 0.5 °, respectively; and 64.9% and 89.5% had a roughness lower than 0.1 and 0.5 m, respectively (where roughness is defined as the standard deviation of the orthogonal residuals). Qualitatively, our new slope and roughness maps display a wealth of glaciological information, including ice shelf flow patterns and the locations of megadune fields in East Antarctica. These findings enhance our

480 understanding of the AIS's geometrical properties and represent, to the best of our knowledge, the first continent-wide analysis of Antarctic surface roughness, that is independent of slope.

During operation, the Sentinel-3 onboard tracker aims to position the L1b range window so that it captures the underlying topographic surface. One way to measure its successes in doing so, is to assess the proportion of the surface illuminated by the instrument that falls within the range window. Performing such an assessment at the ice sheet scale, through the analysis of

485 over 8 million echoes, we find that in 23.7% of cases, capturing the full topography within the beam footprint is impossible, due to the relatively small ~60 m L1b range window of Sentinel-3, relative to the high topographic variance found across some regions of the ice sheet. Building on this, we also investigated the performance of the current window placement, by measuring the ratio of actual topographic capture to the maximum possible capture that could be achieved with an adjusted position of the range window. On average, the current placement achieved a median of 89.7 ± 3.27% of total possible topographic capture,

490 with this value decreasing with increasing slope and roughness. This analysis can inform further refinement of the Sentinel-3

tracker, and also serve to support the design of future missions, by providing empirical information to optimise the size and positioning of the range window.

Within the Level-2 Sentinel-3 altimetry product, an assumption is made that the echoing point (the so-called POCA) lies within the intersection of the range window and the beam limited footprint. To investigate this assumption, we classified the location of the specified L2 POCA, along with our own POCA that was derived by minimising the range to the illuminated REMA surface, relative to the position of the Sentinel-3 L1b range window. We found that the assumption that the L2 POCA falls within the range window was correct for 89.4% of the data, with failures becoming more common with increasing slope and roughness. Our Roemer-derived echoing points exhibited similar patterns to that of the L2, with POCA being captured by the range window in 89.0% of cases. From this analysis, it is clear that for ∼10% of the ice sheet, in regions of more complex topography, the algorithms used to relocate the echo can be improved.

Finally, we explored the correlation between sequences of altimetry echoes along the satellite orbit track, to provide a first assessment of how surface topography affects waveform decorrelation. We found that inter-record correlation was generally high, but decreased in areas with complex topography. Similarly, taking the larger-scale correlation change across 50-records (spanning ∼15 km) indicated that the rate of decorrelation was more rapid in regions with high surface slope and roughness. This analysis therefore provides direct evidence of the relationship between surface topography and altimetry echo correlation at the ice sheet scale, thereby enhancing our understanding of this dependency. This study has shown how a new generation of high-resolution DEMs can be used to assess and understand the performance of current altimetry in-flight systems and on-the-ground processing. This information provides new insight to help understand the current performance of the Sentinel-3 fleet of satellite altimeters, and also serves as a template for future analysis that can guide the design and optimisation of planned missions such as the Copernicus Polar Ice and Snow Topography Altimeter (CRISTAL).

Author contributions. MM conceived the study, MM and JP designed the work, JP performed the analysis, and MM and JP wrote the manuscript.

Competing interests. The authors declare that they have no conflict of interest.

References

515 Abdalla, S., Abdeh Kolahchi, A., Ablain, M., Adusumilli, S., Aich Bhowmick, S., Alou-Font, E., Amarouche, L., Andersen, O. B., Antich, H., Aouf, L., Arbic, B., Armitage, T., Arnault, S., Artana, C., Aulicino, G., Ayoub, N., Badulin, S., Baker, S., Banks, C., Bao, L., Barbetta, S., Barceló-Llull, B., Barlier, F., Basu, S., Bauer-Gottwein, P., Becker, M., Beckley, B., Bellefond, N., Belonenko, T., Benkiran, M., Benkouider, T., Bennartz, R., Benveniste, J., Bercher, N., Berge-Nguyen, M., Bettencourt, J., Blarel, F., Blazquez, A., Blumstein, D., Bonnefond, P., Borde, F., Bouffard, J., Boy, F., Boy, J.-P., Brachet, C., Brasseur, P., Braun, A., Brocca, L., Brockley, D., Brodeau, L.,

520 Brown, S., Bruinsma, S., Bulczak, A., Buzzard, S., Cahill, M., Calmant, S., Calzas, M., Camici, S., Cancet, M., Capdeville, H., Carabajal, C. C., Carrere, L., Cazenave, A., Chassignet, E. P., Chauhan, P., Cherchali, S., Chereskin, T., Cheymol, C., Ciani, D., Cipollini, P., Cirillo, F., Cosme, E., Coss, S., Cotroneo, Y., Cotton, D., Couhert, A., Coutin-Faye, S., Crétaux, J.-F., Cyr, F., d'Ovidio, F., Darrozes, J., David, C., Dayoub, N., De Staerke, D., Deng, X., Desai, S., Desjonqueres, J.-D., Dettmering, D., Di Bella, A., Díaz-Barroso, L., Dibarboure, G., Dieng, H. B., Dinardo, S., Dobslaw, H., Dodet, G., Doglioli, A., Domeneghetti, A., Donahue, D., Dong, S., Donlon, C., Dorandeu,

525 J., Drezen, C., Drinkwater, M., Du Penhoat, Y., Dushaw, B., Egido, A., Erofeeva, S., Escudier, P., Esselborn, S., Exertier, P., Fablet, R., Falco, C., Farrell, S. L., Faugere, Y., Femenias, P., Fenoglio, L., Fernandes, J., Fernández, J. G., Ferrage, P., Ferrari, R., Fichen, L., Filippucci, P., Flampouris, S., Fleury, S., Fornari, M., Forsberg, R., Frappart, F., laure Frery, M., Garcia, P., Garcia-Mondejar, A., Gaudelli, J., Gaultier, L., Getirana, A., Gibert, F., Gil, A., Gilbert, L., Gille, S., Giulicchi, L., Gómez-Enri, J., Gómez-Navarro, L., Gommenginger, C., Gourdeau, L., Griffin, D., Groh, A., Guerin, A., Guerrero, R., Guinle, T., Gupta, P., Gutknecht, B. D., Hamon, M., Han, G., Hauser,

530 D., Helm, V., Hendricks, S., Hernandez, F., Hogg, A., Horwath, M., Idžanović, M., Janssen, P., Jeansou, E., Jia, Y., Jia, Y., Jiang, L., Johannessen, J. A., Kamachi, M., Karimova, S., Kelly, K., Kim, S. Y., King, R., Kittel, C. M., Klein, P., Klos, A., Knudsen, P., Koenig, R., Kostianoy, A., Kouraev, A., Kumar, R., Labroue, S., Lago, L. S., Lambin, J., Lasson, L., Laurain, O., Laxenaire, R., Lázaro, C., Le Gac, S., Le Sommer, J., Le Traon, P.-Y., Lebedev, S., Léger, F., Legresy, B., Lemoine, F., Lenain, L., Leuliette, E., Levy, M., Lillibridge, J., Liu, J., Llovel, W., Lyard, F., Macintosh, C., Makhoul Varona, E., Manfredi, C., Marin, F., Mason, E., Massari, C., Mavrocordatos,

535 C., Maximenko, N., McMillan, M., Medina, T., Melet, A., Meloni, M., Mertikas, S., Metref, S., Meyssignac, B., Minster, J.-F., Moreau, T., Moreira, D., Morel, Y., Morrow, R., Moyard, J., Mulet, S., Naeije, M., Nerem, R. S., Ngodock, H., Nielsen, K., Øie Nilsen, J. E., Niño, F., Nogueira Loddo, C., Noûs, C., Obligis, E., Otosaka, I., Otten, M., Oztunali Ozbahceci, B., P. Raj, R., Paiva, R., Paniagua, G., Paolo, F., Paris, A., Pascual, A., Passaro, M., Paul, S., Pavelsky, T., Pearson, C., Penduff, T., Peng, F., Perosanz, F., Picot, N., Piras, F., Poggiali, V., Étienne Poirier, Ponce de León, S., Prants, S., Prigent, C., Provost, C., Pujol, M.-I., Qiu, B., Quilfen, Y., Rami, A., Raney,

540 R. K., Raynal, M., Remy, E., Rémy, F., Restano, M., Richardson, A., Richardson, D., Ricker, R., Ricko, M., Rinne, E., Rose, S. K., Rosmorduc, V., Rudenko, S., Ruiz, S., Ryan, B. J., Salaün, C., Sanchez-Roman, A., Sandberg Sørensen, L., Sandwell, D., Saraceno, M., Scagliola, M., Schaeffer, P., Scharffenberg, M. G., Scharroo, R., Schiller, A., Schneider, R., Schwatke, C., Scozzari, A., Ser-giacomi, E., Seyler, F., Shah, R., Sharma, R., Shaw, A., Shepherd, A., Shriver, J., Shum, C., Simons, W., Simonsen, S. B., Slater, T., Smith, W., Soares, S., Sokolovskiy, M., Soudarin, L., Spatar, C., Speich, S., Srinivasan, M., Srokosz, M., Stanev, E., Staneva, J., Steunou, N.,

545 Stroeve, J., Su, B., Sulistioadi, Y. B., Swain, D., Sylvestre-baron, A., Taburet, N., Tailleux, R., Takayama, K., Tapley, B., Tarpanelli, A., Tavernier, G., Testut, L., Thakur, P. K., Thibaut, P., Thompson, L., Tintoré, J., Tison, C., Tourain, C., Tournadre, J., Townsend, B., Tran, N., Trilles, S., Tsamados, M., Tseng, K.-H., Ubelmann, C., Uebbing, B., Vergara, O., Verron, J., Vieira, T., Vignudelli, S., Vinogradova Shiffer, N., Visser, P., Vivier, F., Volkov, D., von Schuckmann, K., Vuglinskii, V., Vuilleumier, P., Walter, B., Wang, J., Wang, C., Watson, C., Wilkin, J., Willis, J., Wilson, H., Woodworth, P., Yang, K., Yao, F., Zaharia, R., Zakharova, E., Zaron, E. D., Zhang, Y., Zhao, Z.,

550 Zinchenko, V., and Zlotnicki, V.: Altimetry for the future: Building on 25 years of progress, Advances in Space Research, 68, 319–363, https://doi.org/https://doi.org/10.1016/j.asr.2021.01.022, 2021.

Aublanc, J., Boy, F., Borde, F., and Féménias, P.: A facet based numerical model to retrieve ice sheet topography from Sentinel-3 altimetry, EGUsphere, 2024, 1–26, https://doi.org/10.5194/egusphere-2024-1323, 2024.

Blarel, F., Frappart, F., Legrésy, B., Blumstein, D., Rémy, F., Fatras, C., Mougin, E., Papa, F., Prigent, C., Niño, F., et al.: Altimetry backscat-
555 tering signatures at Ku and S bands over land and ice sheets, in: Remote Sensing for Agriculture, Ecosystems, and Hydrology XVII, vol. 9637, pp. 315–324, SPIE, https://doi.org/10.1117/12.2194498, 2015.

Brenner, A. C., Blndschadler, R. A., Thomas, R. H., and Zwally, H. J.: Slope-induced errors in radar altimetry over continental ice sheets, Journal of Geophysical Research: Oceans, 88, 1617–1623, https://doi.org/10.1029/JC088iC03p01617, 1983.

Brenner, A. C., DiMarzio, J. P., and Zwally, H. J.: Precision and Accuracy of Satellite Radar and Laser Altimeter Data Over the Continental
560 Ice Sheets, IEEE Transactions on Geoscience and Remote Sensing, 45, 321–331, https://doi.org/10.1109/TGRS.2006.887172, 2007.

Brown, G.: The average impulse response of a rough surface and its applications, IEEE Transactions on Antennas and Propagation, 25, 67–74, https://doi.org/10.1109/TAP.1977.1141536, 1977.

Chartrand, A. M. and Howat, I. M.: Basal Channel Evolution on the Getz Ice Shelf, West Antarctica, Journal of Geophysical Research: Earth Surface, 125, e2019JF005 293, https://doi.org/10.1029/2019JF005293, e2019JF005293 2019JF005293, 2020.

565 Chuter, S. J. and Bamber, J. L.: Antarctic ice shelf thickness from CryoSat-2 radar altimetry, Geophysical Research Letters, 42, 10,721–10,729, https://doi.org/https://doi.org/10.1002/2015GL066515, 2015.

Clerc, S., Donlon, C., Borde, F., Lamquin, N., Hunt, S. E., Smith, D., McMillan, M., Mittaz, J., Woolliams, E., Hammond, M., Banks, C., Moreau, T., Picard, B., Raynal, M., Rieu, P., and Guérou, A.: Benefits and Lessons Learned from the Sentinel-3 Tandem Phase, Remote Sensing, 12, https://doi.org/10.3390/rs12172668, 2020a.

570 Clerc, S., Donlon, C., Borde, F., Lamquin, N., Hunt, S. E., Smith, D., McMillan, M., Mittaz, J., Woolliams, E., Hammond, M., et al.: Benefits and lessons learned from the Sentinel-3 tandem phase, Remote Sensing, 12, 2668, https://doi.org/10.3390/rs12172668, 2020b.

Curlander, J. C. and McDonough, R. N.: Synthetic aperture radar, vol. 11, Wiley, New York, 1991.

Davis, C. H., Li, Y., McConnell, J. R., Frey, M. M., and Hanna, E.: Snowfall-Driven Growth in East Antarctic Ice Sheet Mitigates Recent Sea-Level Rise, Science, 308, 1898–1901, https://doi.org/10.1126/science.1110662, 2005.

575 Dawson, G. J. and Bamber, J. L.: Antarctic Grounding Line Mapping From CryoSat-2 Radar Altimetry, Geophysical Research Letters, 44, 11,886–11,893, https://doi.org/https://doi.org/10.1002/2017GL075589, 2017.

Donlon, C., Berruti, B., Buongiorno, A., Ferreira, M.-H., Féménias, P., Frerick, J., Goryl, P., Klein, U., Laur, H., Mavrocordatos, C., et al.: The global monitoring for environment and security (GMES) sentinel-3 mission, Remote sensing of Environment, 120, 37–57, https://doi.org/10.1016/j.rse.2011.07.024, 2012a.

580 Donlon, C., Berruti, B., Mecklenberg, S., Nieke, J., Rebhan, H., Klein, U., Buongiorno, A., Mavrocordatos, C., Frerick, J., Seitz, B., et al.: The sentinel-3 mission: Overview and status, in: 2012 IEEE International Geoscience and Remote Sensing Symposium, pp. 1711–1714, IEEE, https://doi.org/10.1109/IGARSS.2012.6351194, 2012b.

Ehlers, F., Schlembach, F., Kleinherenbrink, M., and Slobbe, C.: Validity assessment of SAMOSA retracking for fully-focused SAR altimeter waveforms, Advances in Space Research, 71, 1377–1396, https://doi.org/10.1016/j.asr.2022.11.034, 2023.

585 Frederikse, T., Buchanan, M. K., Lambert, E., Kopp, R. E., Oppenheimer, M., Rasmussen, D., and Wal, R. S. v. d.: Antarctic Ice Sheet and emission scenario controls on 21st-century extreme sea-level changes, Nature communications, 11, 390, https://doi.org/10.1038/s41467-019-14049-6, 2020.

Griggs, J. and Bamber, J.: Antarctic ice-shelf thickness from satellite radar altimetry, Journal of Glaciology, 57, 485–498, https://doi.org/10.3189/002214311796905659, 2011.

Helm, V., Humbert, A., and Miller, H.: Elevation and elevation change of Greenland and Antarctica derived from CryoSat-2, The Cryosphere, 8, 1539–1559, https://doi.org/10.5194/tc-8-1539-2014, 2014.

Horn, B. K. and Schunck, B. G.: Determining optical flow, Artificial Intelligence, 17, 185–203, https://doi.org/10.1016/0004-3702(81)90024-2, 1981.

Howat, I., Morin, P., Porter, C., and Noh, M.-J.: The Reference Elevation Model of Antarctica, Version 1, https://doi.org/10.7910/DVN/SAIK8B, 2018.

Howat, I. M., Porter, C., Smith, B. E., Noh, M.-J., and Morin, P.: The Reference Elevation Model of Antarctica, The Cryosphere, 13, 665–674, https://doi.org/10.5194/tc-13-665-2019, 2019.

Huang, Q., McMillan, M., Muir, A., Phillips, J., and Slater, T.: Multipeak retracking of radar altimetry waveforms over ice sheets, Remote Sensing of Environment, 303, 114 020, https://doi.org/https://doi.org/10.1016/j.rse.2024.114020, 2024.

Kovaly, J. J.: Synthetic aperture radar, Dedham, 1976.

Levinsen, J. F., Simonsen, S. B., Sørensen, L. S., and Forsberg, R.: The Impact of DEM Resolution on Relocating Radar Altimetry Data Over Ice Sheets, IEEE Journal of Selected Topics in Applied Earth Observations and Remote Sensing, 9, 3158–3163, https://doi.org/10.1109/JSTARS.2016.2587684, 2016.

Li, W., Slobbe, C., and Lhermitte, S.: A leading-edge-based method for correction of slope-induced errors in ice-sheet heights derived from radar altimetry, The Cryosphere, 16, 2225–2243, https://doi.org/10.5194/tc-16-2225-2022, 2022.

Liu, M., Wang, Z., Zhang, B., Wu, S., and An, J.: Extraction and Analysis of the Antarctic Ice Shelf Basal Channel, IEEE Geoscience and Remote Sensing Letters, 20, 1–5, https://doi.org/10.1109/LGRS.2023.3304350, 2023.

Love, A.: In memory of Carl A. Wiley, IEEE Antennas and Propagation Society Newsletter, 27, 17–18, https://doi.org/10.1109/MAP.1985.27810, 1985.

McMillan, M., Muir, A., Shepherd, A., Escolà, R., Roca, M., Aublanc, J., Thibaut, P., Restano, M., Ambrozio, A., and Benveniste, J.: Sentinel-3 delay-Doppler altimetry over Antarctica, The Cryosphere, 13, 709–722, https://doi.org/10.5194/tc-13-709-2019, 2019.

McMillan, M., Muir, A., and Donlon, C.: Brief communication: Ice sheet elevation measurements from the Sentinel-3A and Sentinel-3B tandem phase, The Cryosphere, 15, 3129–3134, https://doi.org/10.5194/tc-15-3129-2021, 2021.

Mertikas, S., Tripolitsiotis, A., Donlon, C., Mavrocordatos, C., Féménias, P., Borde, F., Frantzis, X., Kokolakis, C., Guinle, T., Vergos, G., et al.: The ESA Permanent Facility for altimetry calibration: Monitoring performance of radar altimeters for Sentinel-3A, Sentinel-3B and Jason-3 using transponder and sea-surface calibrations with FRM standards, Remote Sensing, 12, 2642, https://doi.org/10.3390/rs12162642, 2020.

Otosaka, I. N., Shepherd, A., Ivins, E. R., Schlegel, N.-J., Amory, C., van den Broeke, M. R., Horwath, M., Joughin, I., King, M. D., Krinner, G., Nowicki, S., Payne, A. J., Rignot, E., Scambos, T., Simon, K. M., Smith, B. E., Sørensen, L. S., Velicogna, I., Whitehouse, P. L., A, G., Agosta, C., Ahlstrøm, A. P., Blazquez, A., Colgan, W., Engdahl, M. E., Fettweis, X., Forsberg, R., Gallée, H., Gardner, A., Gilbert, L., Gourmelen, N., Groh, A., Gunter, B. C., Harig, C., Helm, V., Khan, S. A., Kittel, C., Konrad, H., Langen, P. L., Lecavalier, B. S., Liang, C.-C., Loomis, B. D., McMillan, M., Melini, D., Mernild, S. H., Mottram, R., Mouginot, J., Nilsson, J., Noël, B., Pattle, M. E., Peltier, W. R., Pie, N., Roca, M., Sasgen, I., Save, H. V., Seo, K.-W., Scheuchl, B., Schrama, E. J. O., Schröder, L., Simonsen, S. B., Slater, T., Spada, G., Sutterley, T. C., Vishwakarma, B. D., van Wessem, J. M., Wiese, D., van der Wal, W., and Wouters, B.: Mass balance of the Greenland and Antarctic ice sheets from 1992 to 2020, Earth System Science Data, 15, 1597–1616, https://doi.org/10.5194/essd-15-1597-2023, 2023.

Passaro, M., Rautiainen, L., Dettmering, D., Restano, M., Hart-Davis, M. G., Schlembach, F., Särkkä, J., Müller, F. L., Schwatke, C., and Benveniste, J.: Validation of an Empirical Subwaveform Retracking Strategy for SAR Altimetry, Remote Sensing, 14, https://doi.org/10.3390/rs14164122, 2022.

Price, S. F., Payne, A. J., Howat, I. M., and Smith, B. E.: Committed sea-level rise for the next century from Greenland ice sheet dynamics during the past decade, Proceedings of the National Academy of Sciences, 108, 8978–8983, https://doi.org/10.1073/pnas.1017313108, 2011.

Pritchard, H., Luthcke, S., and Fleming, A.: Understanding ice-sheet mass balance: progress in satellite altimetry and gravimetry, Journal of Glaciology, 56, 1151–1161, https://doi.org/10.3189/002214311796406194, 2010.

Quartly, G. D., Nencioli, F., Raynal, M., Bonnefond, P., Nilo Garcia, P., Garcia-Mondéjar, A., Flores de la Cruz, A., Crétaux, J.-F., Taburet, N., Frery, M.-L., et al.: The roles of the S3MPC: Monitoring, validation and evolution of Sentinel-3 altimetry observations, Remote Sensing, 12, 1763, https://doi.org/10.3390/rs12111763, 2020a.

Quartly, G. D., Nencioli, F., Raynal, M., Bonnefond, P., Nilo Garcia, P., Garcia-Mondéjar, A., Flores de la Cruz, A., Crétaux, J.-F., Taburet, N., Frery, M.-L., Cancet, M., Muir, A., Brockley, D., McMillan, M., Abdalla, S., Fleury, S., Cadier, E., Gao, Q., Escorihuela, M. J., Roca, M., Bergé-Nguyen, M., Laurain, O., Bruniquel, J., Féménias, P., and Lucas, B.: The Roles of the S3MPC: Monitoring, Validation and Evolution of Sentinel-3 Altimetry Observations, Remote Sensing, 12, https://doi.org/10.3390/rs12111763, 2020b.

Raney, R.: The delay/Doppler radar altimeter, IEEE Transactions on Geoscience and Remote Sensing, 36, 1578–1588, https://doi.org/10.1109/36.718861, 1998.

Ray, C., Martin-Puig, C., Clarizia, M. P., Ruffini, G., Dinardo, S., Gommenginger, C., and Benveniste, J.: SAR Altimeter Backscattered Waveform Model, IEEE Transactions on Geoscience and Remote Sensing, 53, 911–919, https://doi.org/10.1109/TGRS.2014.2330423, 2015.

Remy, F., Mazzega, P., Houry, S., Brossier, C., and Minster, J.: Mapping of the Topography of Continental Ice by Inversion of Satellite-altimeter Data, Journal of Glaciology, 35, 98–107, https://doi.org/10.3189/002214389793701419, 1989.

Rignot, E., Mouginot, J., and Scheuchl, B.: Antarctic grounding line mapping from differential satellite radar interferometry, Geophysical Research Letters, 38, https://doi.org/https://doi.org/10.1029/2011GL047109, 2011.

Rignot, E., Mouginot, J., Scheuchl, B., Van Den Broeke, M., Van Wessem, M. J., and Morlighem, M.: Four decades of Antarctic Ice Sheet mass balance from 1979–2017, Proceedings of the National Academy of Sciences, 116, 1095–1103, https://doi.org/10.1073/pnas.1812883116, 2019.

Riley, S., Degloria, S., and Elliot, S.: A Terrain Ruggedness Index that Quantifies Topographic Heterogeneity, Internation Journal of Science, 5, 23–27, 1999.

Roemer, S., Legrésy, B., Horwath, M., and Dietrich, R.: Refined analysis of radar altimetry data applied to the region of the subglacial Lake Vostok/Antarctica, Remote Sensing of Environment, 106, 269–284, https://doi.org/10.1016/j.rse.2006.02.026, 2007.

Rosen, P. A., Hensley, S., Joughin, I. R., Li, F. K., Madsen, S. N., Rodriguez, E., and Goldstein, R. M.: Synthetic aperture radar interferometry, Proceedings of the IEEE, 88, 333–382, https://doi.org/10.1109/5.838084, 2000.

S3-MPC: Sentinel-3 SRAL Land User Handbook, https://sentinels.copernicus.eu/documents/247904/4871083/Sentinel-3+SRAL+Land+User+Handbook+V1.1.pdf/ebd1444d-240f-70ab-f8fc-e84b67b022cd?t=1673614240693, 2022.

Shepherd, A., Wingham, D., and Rignot, E.: Warm ocean is eroding West Antarctic Ice Sheet, Geophysical Research Letters, 31, https://doi.org/10.1029/2004GL021106, 2004.

Shepherd, A., Gilbert, L., Muir, A. S., Konrad, H., McMillan, M., Slater, T., Briggs, K. H., Sundal, A. V., Hogg, A. E., and Engdahl, M. E.: Trends in Antarctic Ice Sheet Elevation and Mass, Geophysical Research Letters, 46, 8174–8183, https://doi.org/10.1029/2019GL082182, 2019.

Siegert, M. J., Ross, N., and Le Brocq, A. M.: Recent advances in understanding Antarctic subglacial lakes and hydrology, Philosophical Transactions of the Royal Society A: Mathematical, Physical and Engineering Sciences, 374, 20140306, https://doi.org/10.1098/rsta.2014.0306, 2016.

Siegfried, M. R. and Fricker, H. A.: Thirteen years of subglacial lake activity in Antarctica from multi-mission satellite altimetry, Annals of Glaciology, 59, 42–55, https://doi.org/10.1017/aog.2017.36, 2018.

Simonsen, S. B., Barletta, V. R., Colgan, W. T., and Sørensen, L. S.: Greenland Ice Sheet Mass Balance (1992–2020) From Calibrated Radar Altimetry, Geophysical Research Letters, 48, e2020GL091216, https://doi.org/https://doi.org/10.1029/2020GL091216, 2021.

Tilling, R. L., Ridout, A., Shepherd, A., and Wingham, D. J.: Increased Arctic sea ice volume after anomalously low melting in 2013, Nature Geoscience, 8, 643–646, https://doi.org/10.1038/NGEO2489, 2015.

Villadsen, H., Deng, X., Andersen, O. B., Stenseng, L., Nielsen, K., and Knudsen, P.: Improved inland water levels from SAR altimetry using novel empirical and physical retrackers, Journal of Hydrology, 537, 234–247, https://doi.org/10.1016/j.jhydrol.2016.03.051, 2016.

Wilson, M. F. J., O'Connell, B., Brown, C., Guinan, J. C., and Grehan, A. J.: Multiscale Terrain Analysis of Multibeam Bathymetry Data for Habitat Mapping on the Continental Slope, Marine Geodesy, pp. 3–35, https://doi.org/10.1080/01490410701295962, 2007.

Wingham, D., Rapley, C., and D, G.: New Techniques in Satellite Altimeter Tracking Systems, in: IGARSS 86 Symposium, 1986.

Wingham, D. J., Ridout, A. J., Scharroo, R., Arthern, R. J., and Shum, C. K.: Antarctic Elevation Change from 1992 to 1996, Science, 282, 456–458, https://doi.org/10.1126/science.282.5388.456, 1998.

Zevenbergen, L. W. and Thorne, C. R.: Quantitative analysis of land surface topography, Earth Surface Processes and Landforms, 12, 47–56, https://doi.org/10.1002/esp.3290120107, 1987.

Zinck, A.-S. P., Wouters, B., Lambert, E., and Lhermitte, S.: Unveiling spatial variability within the Dotson Melt Channel through high-resolution basal melt rates from the Reference Elevation Model of Antarctica, The Cryosphere, 17, 3785–3801, https://doi.org/10.5194/tc-17-3785-2023, 2023.